Nano-structural stiffness measure for soft biomaterials of heterogeneous elasticity

Shu-Wen W Chen, Jean-Marie Teulon, Harinderbir Kaur, Christian Godon, Jean-Luc Pellequer

ARTICLE

Nano-structural stiffness measure for soft biomaterials of heterogeneous elasticity

Received 00th January 20xx,
Accepted 00th January 20xx

DOI: 10.1039/x0xx00000x

Shu-wen W. Chen*[a,b], Jean-Marie Teulon[a], Harinderbir Kaur[a], Christian Godon[c], and Jean-Luc Pellequer*[a]

Measuring the structural stiffness aims to reveal the impact of nanostructured components or various physiological circumstances on the elastic response of material to an external indentation. With a pyramidal tip at a nano-scale, we employed the atomic force microscopy (AFM) to indent the surfaces of two compositions of polyacrylamide gels with different softness and seedling roots of *Arabidopsis thaliana*. We found that the stiffness curve derived from the measured force exhibits a heterogeneous character in elasticity. According to the tendency of stiffness curve, we decomposed the responding force into depth-impact (F_C), Hookean (F_H) and tip-shape (F_S) components, called trimechanic, and represent their strengths by the respective spring constants (k_C, k_H, k_S) of three parallel-connected spring (3PCS) analogs to differentiate restoring nanomechansims of indented materials. The effective Young's modulus $\hat{E}$ and the total stiffness k_T (= k_H + k_S) globally unambiguously distinguish the softness between the two gel categories. Data fluctuations were observed in the elasticity parameters of individual samples, reflecting nanostructural variations in the gel matrix. Similar tendencies were found in the results from growing plant roots, though the data fluctuations are expectedly much more dramatic. The zone-wise representation of stiffness by the trimechanic-3PCS framework demonstrates a stiffness measure that reflects beneath nanostructures encountered by deepened depth. It provides a new paradigm for analyzing restoring nanomechanics of soft biomaterials in response to indenting forces.

Introduction

Recently, mechanobiology has attracted a great deal of attention on how external forces can regulate the function of proteins, cells, and tissues [1, 2]. In particular, it remains elusive on how cells transduce mechanical stresses, ranging from Pascals to mega Pascals, into physiological processes and end up with serious physiopathological consequences [3]. Many attempts have been made to accurately characterize elastic properties of these soft biomaterials, including micropipette aspiration [4], optical tweezers [5], deformability cytometry [6], Brillouin microscopy [7], and the most adopted strategy, atomic force microscopy (AFM) [8]. AFM indentation results have brought to evidence that certain diseases are subject to abnormal cellular mechanics, for example, a lowered stiffness measured for cancer cells compared to normal ones [9]. Similar results were found in extracellular matrix [10, 11] and tissues during cancer progression [12, 13].

In the instrumental setup of AFM for indentation, the tip attached beneath the micro-sized cantilever plays as an indenter to compress the surface of cells or tissues. In this process, cantilever deflections are recorded as the so-called force-displacement data [14, 15], from which the Young's modulus is deduced [16]. In assessment of the Young's modulus, Hertzian [17] and Sneddon's models [18] are the two widely used to analyze the force-depth data acquired by AFM. The latter delineates the relation between the responding force of material and the indented depth, which depends on the shape of AFM tip. Hence, various shapes of tip have been exploited to study the tip-shape effect on the magnitude of Young's modulus [19, 20]. In practice, these models assume that the material is elastically homogeneous and the pursuit of one Young's modulus is sufficient for characterizing its elastic properties.

The architecture of cells and tissues is by essence complex and non-homogeneous [21, 22]. Although stiffness measure mainly

[a] Univ. Grenoble Alpes, CEA, CNRS, IBS, F-38000 Grenoble, France
[b] Rue Cyprien Jullin, Vinay, 38470, France.
[c] Aix Marseille Univ, CEA, CNRS, BIAM, 13108 Saint Paul-Lez-Durance, France
† Footnotes relating to the title and/or authors should appear here.
Electronic Supplementary Information (ESI) available: [details of any supplementary information available should be included here]. See DOI: 10.1039/x0xx00000x

depends on the composition and structured composite of material surface, the so-called bottom-effect [23, 24] or the substratum may alter the stiffening behaviors [25, 26]. The deformation of nano-structured component caused by external stresses depends on the bonding network and strengths of its chemical groups. Such a complication in stiffness measure brought by structural complexity makes conventional models difficult in interpretation of measured stiffness, especially in the study of soft biomaterials [27]. Therefore, a full analysis over the entire indentation trajectory is needed for our understanding on the above-mentioned issues. Here, we propose a robust strategy, coined trimechanic theory, to encompass elastic behaviors of soft- and bio-materials in various circumstances. Analogous to a vector basis spanning a vector space, a mechanics basis formed of three elements spans the nanomechanics space in the trimechanic theory. Every elastic response can be written as a linear combination of the three basis nanomechanics. Difference in the elastic behaviors or elasticity heterogeneity of material can be quantified by their strengths. In this article, we illustrate the concept and application of the trimechanic theory to the force measurements from AFM indentation.

Methodology

A. Theory and model

A. 1. Indentation force and stiffness

Consider the depth and force measurements by AFM indentation as a sequence of time events, $Z(t)$ and $F_T(t)$, in a duration of T. During this period, the material is assumed to behave as a homogeneous elastic body, implying that the elastic property of the material can be characterized by one single Young's modulus. In the use of a axisymmetric tip, the Sneddon's solutions to Boussinesq's problem [28] relates the force $F_T(t)$ as a quadratic function of penetrated depth $Z(t)$ [18]. In this work, we employed a tip of pyramidal shape, of which the force-depth relation is given elsewhere [19] as

$$F_T(t) = \hat{\mathrm{E}}\frac{\tan\alpha}{\sqrt{2}}Z(t)^2, \quad (1)$$

where $\hat{E} = E/(1-\eta^2)$, denoted as the effective Young's modulus with E the Young's modulus and η the Poisson's ratio, and α corresponds to the face angle of the squared pyramidal tip. According to Eq. (1), the stiffness $F_T' \equiv \partial F_T/\partial Z$ is a linear function of penetrated depth Z with a proportional constant R_S, thus

$$F_T' = R_S Z = (\sqrt{2}\ \hat{\mathrm{E}}\tan\alpha)\ Z. \quad (2)$$

R_S can be conceived as stiffness rate, scoring the increment of stiffness per indented depth responded by the material, and directly linked to the effective Young's modulus $\hat{E}$.

For a material of homogeneous elasticity, the stiffness curve derived from F_T should be one single linear segment with one R_S or $\hat{E}$ based on the Sneddon's model. Thereby, we exploited this property to explore elastic heterogeneity of material by examining the slope of stiffness curve during an indenting process. The change in R_S reflects a change in $\hat{E}$ as well as the restoring nanomechanics of material. From Eqs. (1-2), F_T and F_T' are both zero at $Z = 0$ — initial boundary conditions for applying the Sneddon's model.

A.2.Trimechanic theory for general elastic response

For a material whose elastic properties vary with indented depth, we assume they exhibit a zone-wise pattern with a cone-like shape of the indenting tip. Within each depth-zone, the data points share similar elastic properties. Explicitly, the restoring force F_T at the total depth D can be expressed as a sequence of force segments:

$$F_T(D) = \sum_{i=1}^{m}\int_{Z_{i-1}}^{Z_i} F_T'\,dZ = F_T(Z_{j-1}) + \sum_{i=j}^{m}\int_{Z_{i-1}}^{Z_i} F_T'\,dZ = F_T(Z_{m-1}) + \int_{Z_{m-1}}^{D} F_T'\,dZ. \quad (3)$$

The limits of integration define a zone-wise region of indented depth; by default, $F_T(Z_0{=}0)$ is zero. For each indented depth-zone, say Zone j, the F_T (cf. the second equality of Eq. (3)) can be expressed as a composite of three force components:

$$F_T(Z) = F_T(Z_{j-1}) + F_T'(Z_{j-1}) \times (Z - Z_{j-1}) + \int_{Z_{j-1}}^{Z}\left[F_T'(y) - F_T'(Z_{j-1})\right]dy. \quad (4)$$

The first component is the force measured at the sub-surface of the zone, Z_{j-1}; it is a constant thus denoted by F_C. In effect, F_C represents the hitherto force against the indenting tip. The second component is a Hookean force, called F_H, with a proportional constant of $F_T'(Z_{j-1})$. Removing F_C and F_H from the total force F_T, the remaining force satisfies the initial boundary conditions for applying the Sneddon's model. We denote this force as F_S to attribute it to the tip shape, from which the magnitude of $\hat{E}$ is deduced. The three force components govern three nanomechanics modes— this is trimechanic theory. Trimechanic theory is the very concept of composite nanomechanics underlying the restoring mechanism of material in the indentation trajectory. Various elastic responses are expressed as a linear combination of the three basis nanomechanics, whose strengths quantify the difference in the elastic behaviors.

A.3. The three parallel-connected spring (3PCS) analogy

To quantify the strengths of the three basis nanomechanics in an elastic response, we designated a device with three parallel-connected spring (3PCS) analogs whose elastic actions represent the three different mechanical modes; see **Fig. 1**. The strength of each nanomechanics is represented by the spring constant of the corresponding spring analog.

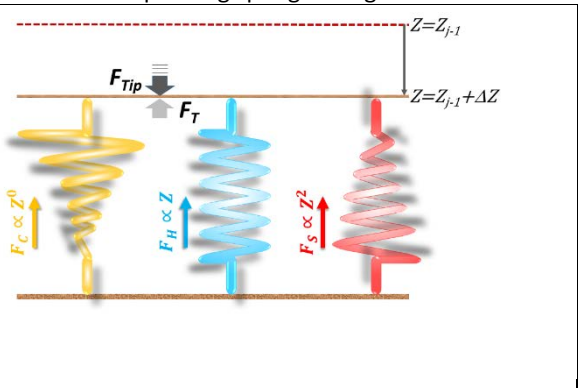

Figure 1: Analogy of three parallel-connected springs: the elastic response (F_T) of a material to an applied force (F_{Tip}) is

a composite action of three nanomechanics, respectively governed by F_C, F_H and F_S, which compose F_T. In the schematic diagram, the tip has arrived at the sub-surface of Zone j in the indentation trajectory, Z_{j-1}, and continues to indent the material with an additional compression, ΔZ. During the indentation from Z_{j-1} to $Z_{j-1}+\Delta Z$, the material exerts a restoring force F_T against the applied force F_{tip} to form, microscopically, a quasi-equilibrium. Except the F_H-spring obeying the Hooke's law, the F_C-curve is a zero-power function of Z, while the nonlinear F_S function, in the diagram, has an exponent of 2 to exemplify the use of a pyramidal tip. The pseudo-stiffness function for the F_C-spring is inversely proportional to the indented depth, picturized by a spring with non-linearly shrinking width. The stiffness function of F_S-spring is proportional to Z, symbolized by a spring with linearly increasing width, and that of F_H-spring is a constant, thus represented by a spring of constant width. According to this spring analogy, $F_T = k_{3PCS}\cdot\Delta Z$, where $k_{3PCS} = k_C + k_H + k_S$, the sum of the spring constants of the three spring devices.

Among the 3PCS analogs, the F_H-spring is the only one having a typical spring constant, $k_{H,j}=F_T'(Z_{j-1})$ for Zone j; it plays the counterpart of F_C in stiffness measure. Two other springs do not have the spring constant, which will be represented by the average of their stiffness function. As a constant, F_C contributes none to stiffness measure. Were there a stiffness function corresponding to F_C, it would be inversely proportional to the amount of compression to make up the force constant. Accordingly, F_C would act like a force thresholder, forbidding the tip without sufficient applied force continuing to indent the material. However, averaging such a pseudo-stiffness function cannot yield a finite number, thus we took $F_T(Z_{j-1})/\Delta Z_j$ as the spring constant of the F_C-spring, $k_{C,j}$, with $\Delta Z_j = Z_j - Z_{j-1}$.

For the F_S-spring, we averaged the corresponding stiffness function (Eq. (2)) over the indented zone and obtained the spring constant:

$$k_{S,j} = R_{S,j}\cdot\Delta Z_j/2 \text{ or } \tan\alpha\cdot\hat{E}_j\cdot\Delta Z_j/\sqrt{2}. \quad (5)$$

We define $k_{T,j} = k_{H,j} + k_{S,j}$ as the stiffness measure for the indented material to represent the stiffness measure for the material indented through the depth-zone j. As shown, the relative strengths of Hookean and tip-shape nanomechanics, $r_{H,j}$ and $r_{S,j}$, are complementary to each other for $r_{H,j} = k_{H,j}/k_{T,j}$ and $r_{S,j} = 1 - r_{H,j}$. Taken together, an elastic response can be fully described by the trimechanic-3PCS framework in a quadruplet format: $[\Delta Z_j, k_{C,j}, k_{T,j}, r_{S,j}]$, the necessary and sufficient parameters to rebuild the fitting curves for F_T and three decomposed force components. Detailed calculations can be found in the supplementary data.

B. Material preparation and AFM instrumentation

B.1. The study systems of soft materials

System 1: The specimen is a 10.4% polyacrylamide gel of about 1.0 mm thickness. For this system, we used a triangular silicon nitride MLCT-BIO-DC cantilever D with nominal k = 0.03 N/m, L = 225 µm, W = 20 µm, F = 15 kHz (Bruker AFM probes, Camarillo, CA, USA), and a squared pyramid shape for the AFM tip with a nominal opening angle of 35°. The ingredient of 10.4% polyacrylamide gel includes 245 µL of acrylamide solution (40%, stored at 4°C, Sigma-Aldrich A8887), 300 µL of Bis-acrylamide (2%, stored at 4°C, Sigma-Aldrich 146072), 1.5 µL of tetramethylenediamine (TEMED, Euromedex, 50406) and 10 µL of ammonium persulfate (APS, 10%, Sigma-Aldrich, A3678) mixed in 443 µL of ultrapure water (MilliQ systems). The gel was assembled as reported previously [29] except that 50 µL of gel were deposited at the center of an O-ring from a polypropylene micro-tube (BRAND®, 780712) which was dipped in Sigmacote® (Sigma-Aldrich, SL2) beforehand.

System 2: The specimen is a 7.4% polyacrylamide gel of about 1.0 mm thickness. The same AFM instrumentation was used as for System 1. The 7.4% polyacrylamide gel was prepared by mixing with 176 µL of acrylamide solution, 210 µL of Bis-acrylamide, 1.5 µL of TEMED, and 10 µL of APS in 602 µL of ultrapure water. The two gel materials were made on the same day.

Experimental setups of AFM for System 1 and 2: We employed an AFM multimode 8 (Bruker, Santa Barbara, CA, USA) equipped with a J-scanner and nanoscope-V controller to perform indentations on gel specimen. The force-displacement measurements were acquired using the force volume mode of the Nanoscope 9.2 software, and the data were collected in a matrix fashion with 8 × 8 or 16 × 16 spots distributed over the material surface in a size of 2 × 2 µm², and each data curve consists of 512 data points with a ramp size smaller than 2 µm.

B.2. The study systems of live tissues

Systems 3-4: The specimens are a 4-day-old seedling root from *Arabidopsis thaliana* with a thickness of about 0.12 mm [30]. The sowing and growing of the plant seeds followed the procedures described elsewhere [31]. In brief, the roots were deposited on a glass covered with pressure sensitive adhesive NuSil MED1-1356 (NuSil Technology LLC, Carpinteria, CA, USA), and kept alive by covering with 200 µL growth solution (MES buffer 3.5 mM, pH 5.5-5.8 with MS liquid medium diluted to 1/10 [32]). The indenter adopted for the system is the triangular pyrex silicon nitride PNP-TR cantilever #2 with nominal k = 0.08 N/m, L = 200 µm, W = 28 µm, F = 17 kHz, which holds a square pyramidal tip with an opening angle of 35° (NanoWorld, Neuchatel, Switzerland).

Experimental setups of AFM for Systems 3-4: The data values were acquired with a Dimension 3100 AFM (Bruker, Santa Barbara, CA, USA) equipped with a hybrid scanner and a nanoscope V controller. We recorded the data in a standard approach of force-distance measurements with the picoforce mode of the Nanoscope 7.3 software. Each data curve composed of 4096 points with a ramp size of 3 µm. All the indentation experiments on plants were performed in a single day.

Results and Discussion.

A. Elastic behaviors of soft materials

We present the results of AFM indentation for two gel composites with different concentrations of acrylamide and bis-acrylamide cross-linker, yet with the same molar ratio of acrylamide to bis-acrylamide, 16:1 (see Methodology). The gel system of higher (10.4%) concentration is presumably stiffer than that of the lower (7.4%) one. The former is thus called hard gel while the latter soft. The F_T-derived stiffness (or non-fitted stiffness) curves of the two gel systems are shown in **Fig. 2a**, rising up with deeper indented depth. However, the stiffness curve of the hard gel rises up faster and reaches a greater magnitude than that of the soft at the same depth, giving the stiffer property to the hard gel. On the surface, the hard gel also exhibits stiffer through its greater stiffness value. The two curves have two linear segments with distinguished R_S values, indicating the entire indentation trajectory can be modeled as two depth-zones with different elasticity. We obtained $R_{S,1}$ = 265 and $R_{S,2}$ = 249 kPa for the hard gel. Similarly, $R_{S,1}$ = 60.5 and $R_{S,2}$ = 27.3 kPa for the soft gel. As seen later, the tendency of $\hat{E}$ would be closely related with that of R_S.

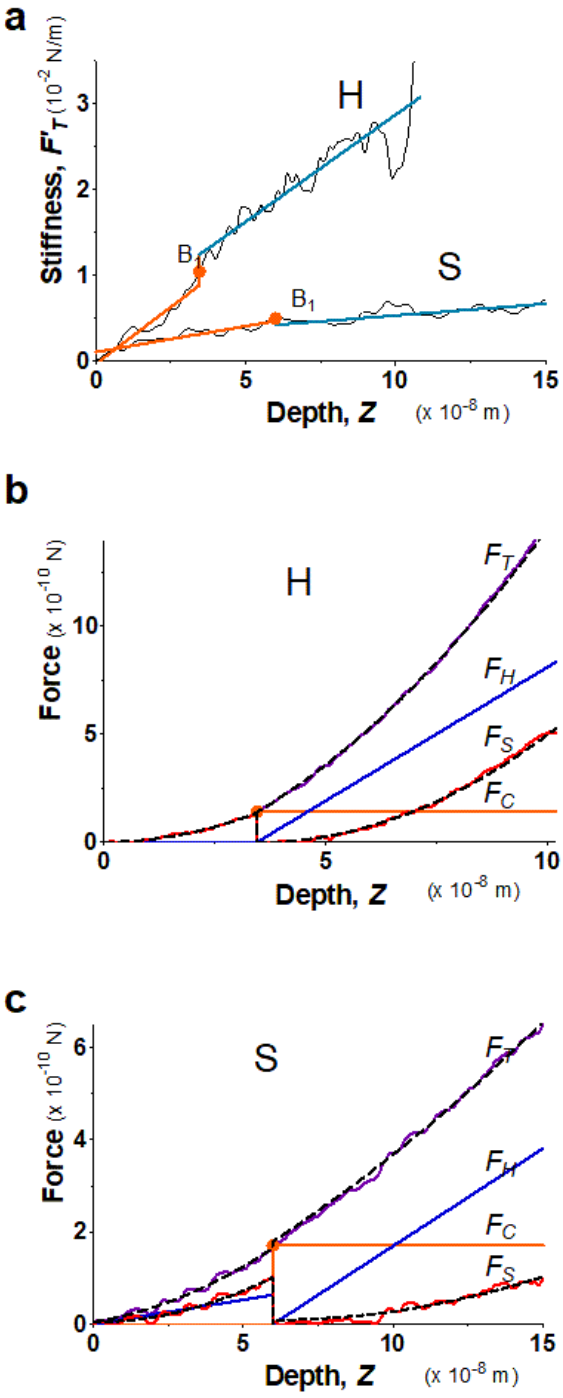

Figure 2: Elastic behaviors of gel materials under the AFM indentation. (a) Stiffness curves of two gel materials with different degrees of softness; "H" labels the hard gel while "S" labels the soft. The black solid lines present the F_T-derived stiffness curves. B_1 is the point breaking the stiffness curve into two segments at a depth of Z_1. Here, Z_1 = 34.6 nm for "H" and Z_1 = 59.9 nm for "S". Each stiffness segment was fitted to a linear function, drawn by an orange line for the first segment and in a light-blue color for the second one. (b) Decompose the restoring force of the hard gel (System 1)

into three force components. F_T, F_C, F_H and F_S-curves are correspondingly presented by magenta, orange, blue and red lines, while fitting curves are drawn by black dashed lines. (c) Decompose the restoring force of the soft gel (System 2) into three force components. Similar to b, F_T, F_C, F_H and F_S are presented by magenta, orange, blue and red lines, respectively. The fitting results are drawn by black dashed lines. The detail of linear segmentation and fitting is referred to Supplementary data.

Fig. 2b and **2c** present the curves of F_T as well as the three force components for the two gel systems. We deduced the $\hat{E}$ values from F_S-curves and obtained $\hat{E}_1$ = 230 and $\hat{E}_2$ = 236 kPa for the hard gel, $\hat{E}_1$ = 54.4 and $\hat{E}_2$ = 23.4 kPa for the soft, showing that the hard gel has greater $\hat{E}$'s globally. We list the values of trimechanic-3PCS quadruplets: for the hard gel, [ΔZ_1, $k_{C,1}$, $k_{T,1}$, $r_{S,1}$] = [34.6, 0.0, 3.92, 1.0] and [ΔZ_2, $k_{C,2}$, $k_{T,2}$, $r_{S,2}$] = [73.6, 1.92, 20.0, 0.41]; for the soft gel, [ΔZ_1, $k_{C,1}$, $k_{T,1}$, $r_{S,1}$] = [59.9, 0.0, 2.66, 0.60] and [ΔZ_2, $k_{C,2}$, $k_{T,2}$, $r_{S,2}$] = [198, 0.86, 6.52, 0.35], where k_C's and k_T's are in the unit of mN/m, ΔZ's in nm and r_S's are dimensionless throughout the paper, unless mentioned otherwise. We found that k_T unambiguously distinguishes the softness between soft and hard gels. As shown for this hard gel sample, the k_S dominates the total stiffness, k_T, in the first depth-zone, while k_H becomes comparable to k_S at the end. Similarly, k_S is greater than k_H for the soft gel during the first depth-zone indentation while it is reverse in the second depth-zone. This behavior is illustrated by the change in r_S value. In either case, k_T steadily increases with deepened depth and accords with the tendency of F_T-derived stiffness curve. The structure of gel material formed by polymerization of acrylamide and bis-acrylamide depends on many factors such as gel concentration, molar ratio, pH and temperature [33, 34]. The k_H and k_S or r_S may provide more detailed information on stiffening progresses of various indented spots of one gel or different gel composites, underlying the change in molecular bonding state of polyacrylamide under the external force. It is noteworthy that an effectively sharp tip should be employed instead of a large colloidal indenter for probing such a structural stiffness of material. For a nanostructured material, large spherical tips lead to a result averaged over heterogeneous elastic properties of the material. Consequently, stiffness variations attributed to different substructures and energetics on a nano-meter scale are often overlooked.

We compared the results from the trimechanic-3PCS model with that from an open-source, the pyramid model of the AtomicJ software [35], which aims to obtain the best fit of the indentation curve to the Sneddon's solution with a single segment by varying the location of the contact point. The fitting results of responding force from our model and AtomicJ-pyramid are shown in **Figs. S2a-b**. Regarding the fitting goodness, the trimechanic-3PCS model yields a perfect fit, whereas AtomicJ-pyramid performed a poor fitting, particularly on the beginning of the indentation curve. From the data of $\hat{E}$ and k_T, it shows that the stiffness of material represented by AtomicJ-pyramid reflects an averaged value rather than the refined structural stiffness provided by the trimechanic-3PCS model. Moreover, the trimechanic-3PCS model provides a stiffness measure, which follows the tendency of the F_T-derived stiffness curve accurately. It indicates that the trimechanic-3PCS model can be used to delineate the change in elasticity of the material in depth.

Beside the illustrating gel samples for the trimechanic-3PCS model shown in **Fig. 2**, we have applied this framework to 91 indentation curves of hard gel and 155 of soft gel; the results of k_T and $\hat{E}$ are presented in a graph format (see **Fig. S3**). It shows that local elastic behaviors of these gel samples are not necessarily identical. Globally, the category of hard gel (upper sections of **Fig. S3a,b**) exhibits a shorter length of indentation trajectory (the horizontal coordinate) yet much stiffer (brighter colors in intensity) than that of soft gel. It reveals that the hard gel accelerates the stiffening process shortly in depth against the deeper indentation by the AFM tip. Subsequently, the variation in the number of depth-zone is somewhat related to elasticity change in the indentation trajectory.

B. Elastic behaviors of live tissues

Biological tissues are often composed of complex structures. The probed surface of seeding roots of *A. thaliana* is formed of the external epidermal cell wall, which is structured with complex intertwining of cellulose, hemicellulose, and pectin [36], including about 40% of water [37]. Two seedling roots (System 3 and 4) were chosen particularly for demonstrating the advantages of using the trimechanic-3PCS model for analyzing elastic responses of live tissues with similar turgor pressure in a condition of constant temperature and buffer medium. In **Fig. 3a**, System 3 exhibits only one linear segment for the stiffness curve while the other five. For the latter system, the slope of F_T-derive stiffness varies gradually that leads to a bent curve, unlike the former one that can be modeled by one straight line. These findings imply the impact of heterogeneous structure on the stiffness measure of plant root tissue, which cannot be modeled as one uniform shell structure [38]. One should acknowledge that the linear segmentation of stiffness curve is based on the present theoretical ground rather than the goodness of numerical fittings. Although System 4 has numerous depth-zones, the total depth of indentation is much shorter than that of System 3, 400 nm vs. ~1 μm. These depths indicate that the indentation was performed within the range of the external epidermal cell wall [39]. **Fig. 3b** and **3c** show their corresponding force curves and the three force components.

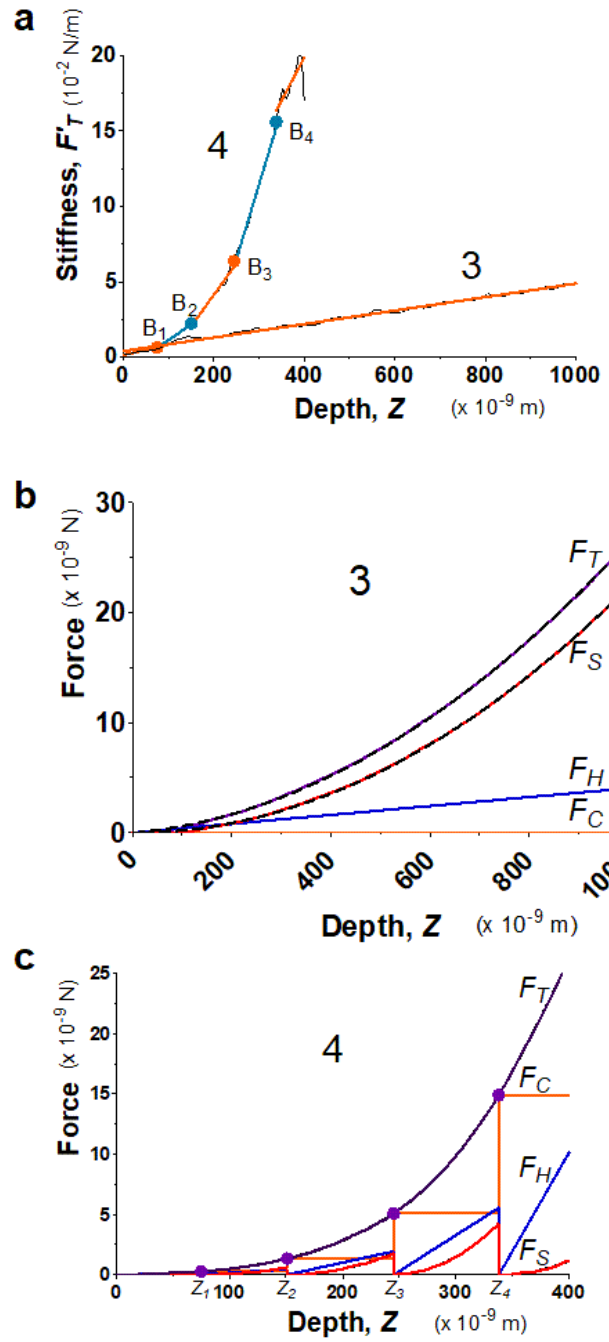

Figure 3: Elastic behaviors of two 4-day-old seedling roots from *A. thaliana* (System 3 and 4) under AFM indentations. (a) The stiffness curves of the two root systems, and labeled by 3 and 4, respectively. The black solid line presents F_T-derived stiffness curves, and the linear fitted segments are indicated by alternating colors, orange and light blue. The Z-coordinates of breaking points for System 4 are Z_1=74.8, Z_2=151, Z_3=245 and Z_4=338 nm. The single R_S of System 3 equals 44.7 kPa, and for the sequential segments of System 4, $R_{S,1}$=67.2, $R_{S,2}$=209, $R_{S,3}$=417, $R_{S,4}$=989, and $R_{S,5}$=570 kPa. (b) Application of trimechanic-3PCS model to System 3. From the F_S curve, the deduced $\hat{E}$ equals 45.2 kPa. The parameters of trimechanic-3PCS quadruplet are ΔZ=1.0 μm, k_T=27.2 mN/m and r_S=0.85 (k_C is omitted). (c) Application of trimechanic-3PCS model to System 4. The trimechanic-3PCS quadruplets for the five depth-zones are: [ΔZ_1, $k_{C,1}$, $k_{T,1}$, $r_{S,1}$] = [74.8, 0.0, 3.93, 0.63], [ΔZ_2, $k_{C,2}$, $k_{T,2}$, $r_{S,2}$] = [76.0, 3.64, 13.9, 0.57], [ΔZ_3, $k_{C,3}$, $k_{T,3}$, $r_{S,3}$] = [94.2, 14.3, 39.4, 0.48], [ΔZ_4, $k_{C,4}$, $k_{T,4}$, $r_{S,4}$] = [92.9, 55.1, 105, 0.43] and [ΔZ_5, $k_{C,5}$, $k_{T,5}$, $r_{S,5}$] = [62.0, 241, 182, 0.1]; see the main text for the units of parameters. The effective Young's moduli are $\hat{E}_1$ = 67.5, $\hat{E}_2$ = 211, $\hat{E}_3$ = 403, $\hat{E}_4$ = 984 and $\hat{E}_5$ = 611 kPa.
All the plots of F_T as well as F_C, F_H and F_S against Z are respectively presented by magenta, orange, blue and red lines. The fitting results are delineated by black dashed lines.

In comparison with AtomicJ-pyramid (**Figs. S2c-d**), we found that when the contact point and force fittings from both models are in good agreement, the deduced effective Young's moduli are unsurprisingly comparable, 45.2 and 45.5 kPa respectively from the trimechanic-3PCS model and AtomicJ-pyramid for System 3. On the contrary, the discrepancy becomes severe between the two models; this can be seen from System 4 (**Fig. S2d**). As mentioned previously, the F_T-derived stiffness curve of this system cannot be modeled as one single linear segment and characterized as of uniform elasticity. Nevertheless, the trimechanic-3PCS model reports the $\hat{E}$ values, ranging from 67.5 to 611 kPa, to describe the elasticity variation with depth. Results for the full plant datasets can be found graphically in **Fig. S3c,d**.

For a live tissue of plant root, the magnitude and variation rate of stiffness with indented depth reflect the change of elastic properties crossing the thickness of the cell wall, which can be further differentiated by the composition of elastic nanomechanics. In particular, the tip-shape nanomechanics (F_S) was found to exert a lower impact on the total response in deeper depth-zones, reflected by a decreased value of r_S or F_S weight. Such deeper indentations render the surface of the material so stiff that the surface hardly deforms itself to accord with the tip shape. One should not naively attribute the discrepancy between the results of trimechanic-3PCS and AtomicJ-pyramid models solely to the different choice of the contact point. We show in **Fig. S1a** that even the contact points determined by the two approaches are close, one still obtains incomparable results.

Conclusions

Trimechanic theory is a straightforward outcome of extending the applicability of the Sneddon's model to the study of elastic heterogeneity. The three force/nanomechanics components, F_C, F_H and F_S, carry information of the impact of hitherto indentation on the material. Excellent fittings of F_T curves by the trimechanic theory indicate that the best use of the Sneddon's model should be restricted to the F_S component instead of the total force F_T, and that the Hookean nanomechanics is substantial in the response. The 3PCS quadruplet [ΔZ, k_C, k_T, r_S] contains all information on characterizing the elastic response

of material, from which the modeled forces along the indentation depth can be reconstructed: $F_T = (k_C+k_T)\bullet\Delta Z$, k_T itself is the extrinsic stiffness, and $\hat{E}$ can be derived from k_T and r_S. Moreover, the combinatory ratio of r_S and r_H alludes to bonding deformability of the composite material. With a nano-sized tip, AFM indentation combined with the trimechanic-3PCS framework provides us a technique to measure the structural stiffness of soft biomaterials, and to quantify the difference of restoring mechanisms from a variety of material conditions. The extended elasticity parameters bring a larger breadth on data comparison than one single parameter, leading to a finer differentiation between elastic properties of materials.

Author Contributions

SWC and JLP conceived the study. SWC developed the theory and performed the computational analysis. JMT designed and made the gels and performed their indentation. HK and CG designed and performed indentation on plant roots. SWC and JLP wrote the manuscript with the contributions of all authors.

Conflicts of interest

"There are no conflicts to declare".

Acknowledgements

IBS acknowledges integration into the Interdisciplinary Research Institute of Grenoble (IRIG, CEA). This work acknowledges the AFM platform at the IBS. Dr Anne-Emmanuelle Foucher (IBS, group EPIGEN) is acknowledged for her contribution to polyacrylamide gels. Dr Thierry Desnos (CEA, BIAM) is acknowledged for his contribution to the *Arabidopsis thaliana* project. Acknowledgment to the ANR project BioPhyt - 18-CE20-0023-03 and the support of the European Union's Horizon 2020 research and innovation programme under the Marie Skłodowska-Curie grant agreement No 812772, Project Phys2BioMed.

Notes and references

1 J. H. Wang and B. P. Thampatty, *Biomech. Model. Mechanobiol.*, 2006, **5**, 1-16.
2 V. Vogel, *Annu. Rev. Physiol.*, 2018, **80**, 353-387.
3 J. F. Stoltz and X. Wang, *Biorheology*, 2002, **39**, 5-10.
4 R. M. Hochmuth, *J. Biomech.*, 2000, **33**, 15-22.
5 H. Zhang and K. K. Liu, *J. R. Soc. Interface*, 2008, **5**, 671-690.
6 O. Otto, P. Rosendahl, A. Mietke, S. Golfier, C. Herold, D. Klaue, S. Girardo, S. Pagliara, A. Ekpenyong, A. Jacobi, M. Wobus, N. Topfner, U. F. Keyser, J. Mansfeld, E. Fischer-Friedrich and J. Guck, *Nat. Methods*, 2015, **12**, 199-202.
7 R. Prevedel, A. Diz-Munoz, G. Ruocco and G. Antonacci, *Nat. Methods*, 2019, **16**, 969-977.
8 M. Krieg, G. Flaschner, D. Alsteens, B. M. Gaub, W. H. Roos, G. J. L. Wuite, H. E. Gaub, C. Gerber, Y. F. Dufrene and D. J. Muller, *Nat. Rev. Phys.*, 2019, **1**, 41-57.
9 M. Lekka, P. Laidler, D. Gil, J. Lekki, Z. Stachura and A. Z. Hrynkiewicz, *Eur. Biophys. J.*, 1999, **28**, 312-316.
10 I. Sokolov, in *Cancer Nanotechnology*, eds. H. S. Nalwa and T. Webster, American Scientific Publishers, 2007, ch. 1, pp. 1-17.
11 S. Kumar and V. M. Weaver, *Cancer Metast. Rev.*, 2009, **28**, 113-127.
12 M. Lekka, K. Pogoda, J. Gostek, O. Klymenko, S. Prauzner-Bechcicki, J. Wiltowska-Zuber, J. Jaczewska, J. Lekki and Z. Stachura, *Micron*, 2012, **43**, 1259-1266.
13 M. Plodinec, M. Loparic, C. A. Monnier, E. C. Obermann, R. Zanetti-Dallenbach, P. Oertle, J. T. Hyotyla, U. Aebi, M. Bentires-Alj, R. Y. Lim and C. A. Schoenenberger, *Nat. Nanotechnol.*, 2012, **7**, 757-765.
14 M. Radmacher, M. Fritz, C. M. Kacher, J. P. Cleveland and P. K. Hansma, *Biophys. J.*, 1996, **70**, 556-567.
15 M. Radmacher, *Meth. Cell Biol.*, 2007, **83**, 347-372.
16 P. Carl and H. Schillers, *Pflugers Archiv.*, 2008, **457**, 551-559.
17 H. Hertz, *C. Vermischte Abhandlungen* 1882, 449-464.
18 I. N. Sneddon, *Int. J. Engng. Sci.*, 1965, **3**, 47-57.
19 F. Rico, P. Roca-Cusachs, N. Gavara, R. Farre, M. Rotger and D. Navajas, *Phys. Rev. E*, 2005, **72**.
20 J. Zemla, J. Bobrowska, A. Kubiak, T. Zielinski, J. Pabijan, K. Pogoda, P. Bobrowski and M. Lekka, *Eur. Biophys. J.*, 2020, **49**, 485-495.
21 S. Kasas, X. Wang, H. Hirling, R. Marsault, B. Huni, A. Yersin, R. Regazzi, G. Grenningloh, B. Riederer, L. Forro, G. Dietler and S. Catsicas, *Cell Motil. Cytoskeleton*, 2005, **62**, 124-132.
22 S. Digiuni, A. Berne-Dedieu, C. Martinez-Torres, J. Szecsi, M. Bendahmane, A. Arneodo and F. Argoul, *Biophys. J.*, 2015, **108**, 2235-2248.
23 E. K. Dimitriadis, F. Horkay, J. Maresca, B. Kachar and R. S. Chadwick, *Biophys. J.*, 2002, **82**, 2798-2810.
24 N. Gavara and R. S. Chadwick, *Nat. Nanotechnol.*, 2012, **7**, 733-736.
25 A. J. Engler, S. Sen, H. L. Sweeney and D. E. Discher, *Cell*, 2006, **126**, 677-689.
26 S. Chiodini, S. Ruiz-Rincon, P. D. Garcia, S. Martin, K. Kettelhoit, I. Armenia, D. B. Werz and P. Cea, *Small*, 2020, **16**, e2000269.
27 D. C. Lin, D. I. Shreiber, E. K. Dimitriadis and F. Horkay, *Biomech. Model. Mechanobiol.*, 2009, **8**, 345-358.
28 J. Boussinesq, *Application des potentiels à l'étude de l'équilibre et du mouvement des solides élastiques, avec des notes étendues sur divers points de physique mathématique et d'analyse*, Gauthier-Villars Imprimeur-Libraire, Paris, 1885.
29 H. Schillers, C. Rianna, J. Schäpe, T. Luque, H. Doschke, M. Wälte, J. J. Uriarte, N. Campillo, G. P. Michanetzis, J. Bobrowska, A. Dumitru, E. T. Herruzo, S. Bovio, P. Parot, M. Galluzzi, A. Podestà, L. Puricelli, S. Scheuring, Y. Missirlis, R. Garcia, M. Odorico, J. M. Teulon, F. Lafont, M. Lekka, F. Rico, A. Rigato, J.-L. Pellequer, H. Oberleithner, D. Navajas and M. Radmacher, *Sci. Rep.*, 2017, **7**, 5117.
30 C. Balzergue, T. Dartevelle, C. Godon, E. Laugier, C. Meisrimler, J.-M. Teulon, A. Creff, M. Bissler, C. Brouchoud, A. Hagège, J. Müller, S. Chiarenza, H. Javot, N. Becuwe-Linka, P. David, B. Péret, E. Delannoy, M.-C. Thibaud, J. Armengaud, S. Abel, J.-L. Pellequer, L. Nussaume and T. Desnos, *Nat. Commun.*, 2017, **8**, 15300.
31 H. Kaur, C. Godon, J.-M. Teulon, T. Desnos and J.-L. Pellequer, in *Mechanics of Cells and Tissues in Diseases*, eds. M. Lekka, D. Navajas, M. Radmacher and A. Podestà, Walter de Gruyter GmbH,, Berlin/Boston, 2022?, vol. 2, pp. 127-140.
32 T. Murashige and F. Skoog, *Physiol. Plant.*, 1962, **15**, 473-497.
33 D. P. Blattler, F. Garner, K. van Slyke and A. Bradley, *J. Chromatogr.*, 1972, **64**, 147-155.
34 A. Rath, F. Cunningham and C. M. Deber, *Proc. Natl. Acad. Sci. USA*, 2013, **110**, 15668–15673.
35 P. Hermanowicz, M. Sarna, K. Burda and H. Gabrys, *Rev. Sci. Instrum.*, 2014, **85**, 063703.

36 P. Albersheim, A. Darvill, K. Roberts, R. Sederoff and A. Staehelin, *Plant cell walls. From chemitry to biology*, Garland Science, Taylor & Francis Group, LLC, New York, NY, USA, 2011.
37 D. Gaff and D. Carr, *Aus. J. Biol. Sci.*, 1961, **14**, 299-311
38 S. Tsugawa, Y. Yamasaki, S. Horiguchi, T. Zhang, T. Muto, Y. Nakaso, K. Ito, R. Takebayashi, K. Okano, E. Akita, R. Yasukuni, T. Demura, T. Mimura, K. Kawaguchi and Y. Hosokawa, *Sci. Rep.*, 2022, **12**, 13044.
39 P. Derbyshire, K. Findlay, M. C. McCann and K. Roberts, *J. Exp. Bot.*, 2007, **58**, 2079-2089.

Supporting information:

Nano-structural stiffness measure for soft biomaterials of heterogeneous elasticity

Shu-wen W. Chen[a,b*], *Jean-Marie Teulon*[a], *Harinderbir Kaur*[a], *Christian Godon*[c], *and Jean-Luc Pellequer*[a*]

[a]Univ. Grenoble Alpes, CEA, CNRS, IBS, F-38000 Grenoble, France

[b]Rue Cyprien Jullin, Vinay, 38470, France.

[c]Aix Marseille Univ, CEA, CNRS, BIAM, 13108 Saint Paul-Lez-Durance, France

Corresponding authors : Shu-wen W. Chen (cmft551@yahoo.com); Jean-Luc Pellequer (jean-luc.pellequer@ibs.fr)

Computational procedure

1. Criteria of being a contact point

Determination of the contact point is the first step for the formation of indentation curve [1]. On a physical view, before reaching the contact point the tip experiences neither force nor force gradient (the first derivative of force) from the material. As a common practice in the study of nanomechanics, the location of the contact point is not pre-determined, it moves with which section of the curve yielding the best fitting results to the mechanical model used. As a consequence, the contact point lost its physical meaning. In this work, we follow the physical fact for determining the contact point, and we do not assume that the study material is necessarily elastically homogeneous.

Before starting with the curve of force (F_d) versus tip-sample separation (z), z being the cantilever-corrected piezo displacement; a small portion (10%) of initial pre-contacting data points are discarded to prevent unacceptable non-flatness and distortions from the baseline. We applied the Savitzky-Golay (SG) filter [2] to alleviate fluctuations of the data series. The great advantage of using the SG filter is not only to smoothen noisy data but also to simultaneously calculate the derivative functions. Basically, the SG filter processes a series of data points in a convolution fashion with a matrix of $(n+1) \times (2w+1)$ convolution coefficients, where w is the half size of the smoothing window, n is the degree of the fitting polynomial function and is the highest order for the derivative function. In this work, we used $n = 3$ and $w = 15$ for all the testing systems. **Fig. S1** describes the detail of locating the contact points (z_c's) of all the study systems based on the criteria, $F_d = 0$ and $\partial F_d/\partial z = 0$.

2. Depth zones of different elastic properties in the indentation trajectory

Once the contact point was decided, we generated the plot of F_T against Z straightforwardly with that $Z = -(z - z_c)$ and $F_T(Z) = F_d(z) - F_d(z_c)$, followed by removals of tip effects. We adopted a stiffness-based approach to identify the regions of different elasticity in the indentation trajectory. The derived stiffness from the measured force is defined as the ratio of $\partial F_T/\partial t$ to $\partial Z/\partial t$, and $\partial F_T/\partial t$ and $\partial Z/\partial t$ were computed using the SG filter. Based on Sneddon's model with the pyramidal tips, the stiffness curve (F_T' vs. Z) would appear as a series of linear segments joined at the breaking points, B_j's. The Z coordinates of B_j's are referred to as generalized contact points that interfaces two adjacent depth-zones of different elastic properties.

The segmentation of stiffness curve was performed using clusterwise linear regression with the

minimal distance method [3]. For a curve of m linear segments, the clusterwise linear regression optimizes all the segments simultaneously with $2m$ fitting parameters. Linearity of two consecutive segments was tested by their intersection angle. If the angle was within 5°, then the two segments were merged together to become one. Each segment required at least $(2w+1)$ data points.

3. Force decomposition for the trimechanic theory

For each stiffness segment yielded from clusterwise linear regression, say Zone j, it has a generic form of linear function: $c_j + R_{S,j} \times Z$ with c_j and $R_{S,j}$ the two fitting parameters, which in turn define the F_H component as $k_{H,j} \times (Z - Z_{j-1})$, where $k_{H,j} = c_j + R_{S,j} \times Z_{j-1}$ and equals $F_T'(Z_{j-1})$ in Eq. (4). More important, the heterogeneity of material elasticity in the indentation trajectory is differentiated by $R_{S,j}$. F_C is set to $F_T(Z_{j-1})$, whereas the F_S component is the total force F_T subtracting the sum of F_C and F_H. In general, F_C and F_H do not need a fitting function, only F_S needs one. For example, F_S will fit to a parabolic function when a cone-like or pyramidal tip is in use: $f_{p,j}(Z - Z_{j-1})^2 + \delta_j$, where $f_{p,j}$ and δ_j are two fitting parameters. The effective Young's modulus can be deduced as $\hat{E}_j = \sqrt{2}\, f_{p,j}/tan(\alpha)$ (cf. Eq. (2)) by ignoring the contribution attributed to the modulus of indenting tip itself. The weight of F_S contribution w_S is defined as $F_S(Z_j)/F_T(Z_j)$ to decide whether F_S to be neglected. If $w_S < 0.1$, then F_S is set to zero. Its data values are joined to F_H and the resultant F_H will be re-fitted to $k_{H,j} \times (Z - Z_{j-1})$, where $k_{H,j}$ now is a fitting parameter instead of an analytical quantity. Consequently, the fitted F_T data values, as presented in **Fig**. **2** and **3**, are the sum of the fitted force and, at most, two other non-fitted ones.

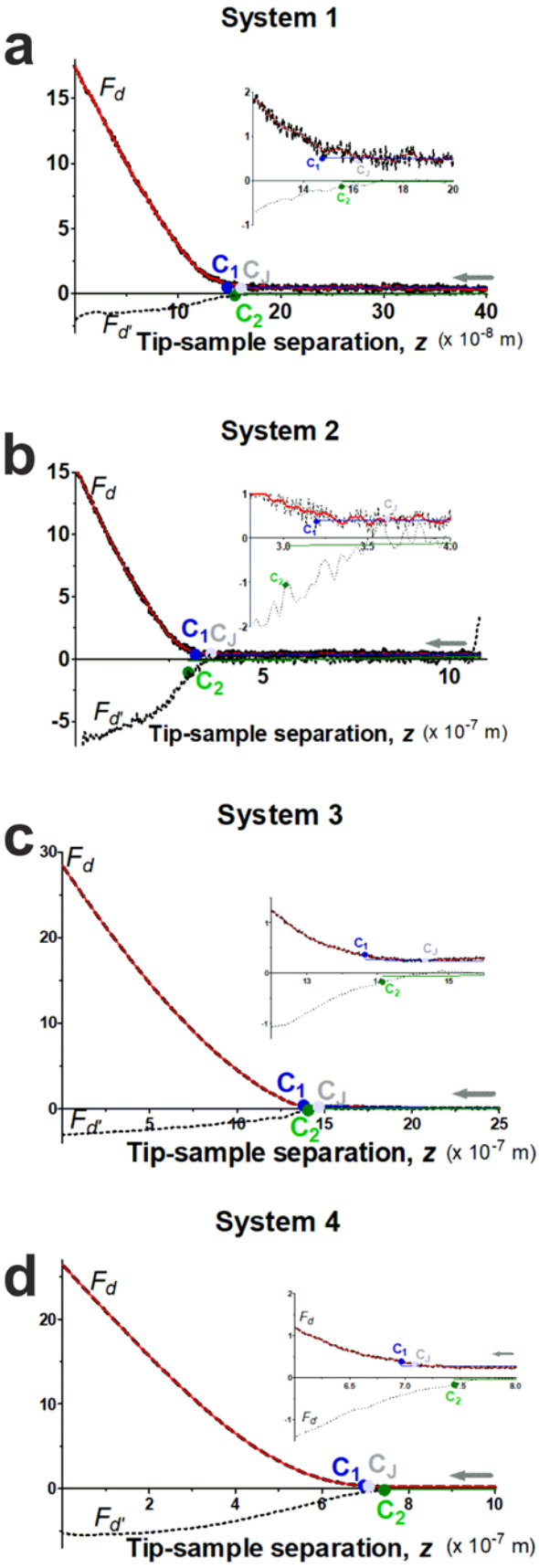
a
System 1
F_d
$F_{d'}$
C_1
C_J
C_2
Tip-sample separation, z (x 10^{-8} m)
b
System 2
F_d
$F_{d'}$
C_1
C_J
C_2
Tip-sample separation, z (x 10^{-7} m)
c
System 3
F_d
$F_{d'}$
C_1
C_J
C_2
Tip-sample separation, z (x 10^{-7} m)
d
System 4
F_d
$F_{d'}$
C_1
C_J
C_2
Tip-sample separation, z (x 10^{-7} m)

Figure S1: Contact points of all the illustrating systems. The determination of contact point is based on the criteria: $F_d(z) = 0$ and $F_d'(z)=0$ (see the main text). The plots of deflection force, $F_d(z)$, and $F_d'(z)$ have been smoothened by the SG filter beforehand and presented by black dashed lines in the figure. Inset graphs illustrate the smoothing effects of the SG filter. Red lines represent smoothed data of $F_d(z)$. The gray arrow along the z coordinate indicates the approaching direction of the tip toward the material surface. The blue and green lines are the baselines obtained by clusterwise linear regression respective to $F_d(z)$ and $F_d'(z)$. Correspondingly, blue and green spots mark the potential contact points along the $F_d(z)$ and $F_d'(z)$ baselines, and denoted by $\mathbf{C_1}$ and $\mathbf{C_2}$. For comparison, gray spots mark the contact point determined by the AtomicJ-pyramid algorithm, and labeled with $\mathbf{C_J}$. In practice, $\mathbf{C_1}$ and $\mathbf{C_2}$ were chosen as close as possible toward the material surface, where $F_d(z_1)$ and $F_d'(z_2)$ are within, 2.5 for gels and 2.9 for plant roots, standard deviations relative to the respective baselines. From our experience, $F_d'(z)$ is better to reflect the tendency of $F_d(z)$ than $F_d(z)$ itself. Consequently, z_2 is taken as the final location of the contact point. The units of F_d and F_d' are in 10^{-7} m, 10^{-8} N, and 10^{-3} N/m, respectively. (**a**) The hard gel (System 1): $z_1 = 14.9$, $z_2 = 14.9$, and $z_J = 16.1$ ($\times 10^{-8}$ m); F_d and F_d' are in 10^{-10} N, and 10^{-2} N/m. (**b**) The soft gel (System 2): $z_1 = 3.19$, $z_2 = 3.01$, and $z_J = 3.62$ ($\times 10^{-7}$ m); F_d and F_d' are in 10^{-10} N and 10^{-3} N/m. (**c**) The plant root of System 3: $z_1 = 13.8$, $z_2 = 14.1$ and $z_J = 14.68$ ($\times 10^{-7}$ m); F_d and F_d' are in 10^{-9} N and 10^{-2} N/m. (**d**) The plant root of System 4: $z_1 = 6.97$, $z_2 = 7.44$ and $z_J = 7.09$ ($\times 10^{-7}$ m); F_d and F_d' are in 10^{-9} N and 10^{-2} N/m.

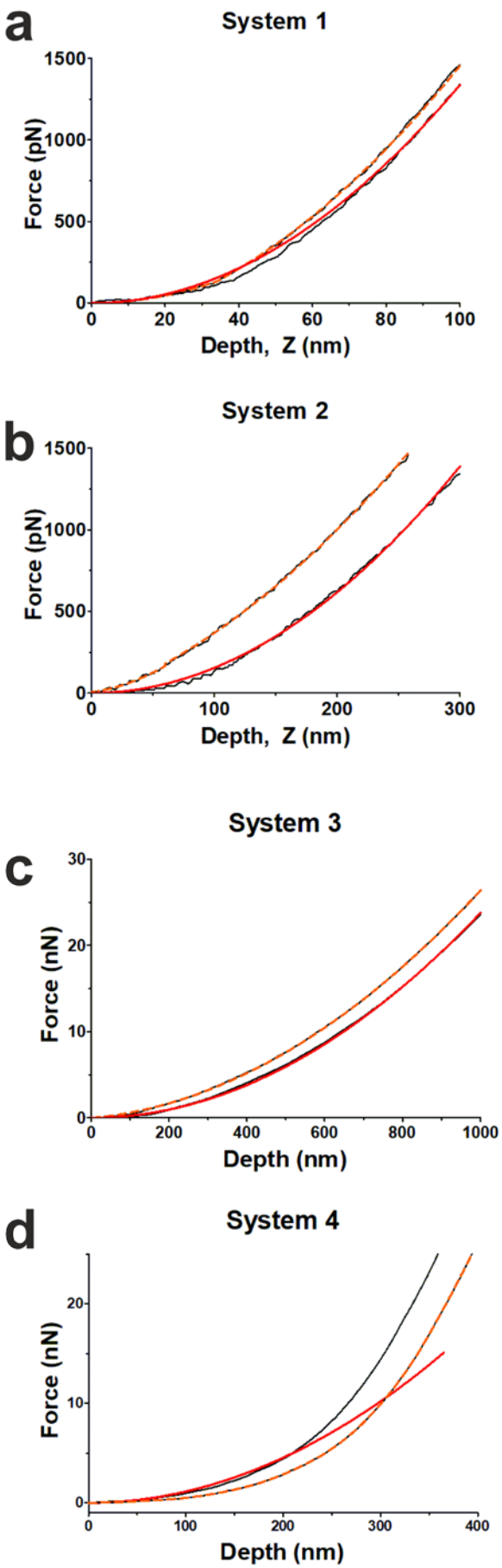
a
System 1
Force (pN)
Depth, Z (nm)
b
System 2
Force (pN)
Depth, Z (nm)
c
System 3
Force (nN)
Depth (nm)
d
System 4
Force (nN)
Depth (nm)

Figure S2: The fitting results of responding force from AtomicJ-pyramid and the trimechanic-3PCS models. The pyramid model of AtomicJ uses the conventional approach to fitting the responding force where the initial contact point is sought for improving the goodness of the fitting by a robust exhaustive method, LTA [4]. In the parameter setup of AtomicJ, the same semi-vertical angle of the pyramidal tip, 35˚, and a Poisson ratio of 0.0 were used for best comparison with the tri-mechanic-3PCS model to illustrate different consequences from the conventional usage of the Sneddon's model and our strategy. Derived indentation curves from AFM measurements are drawn by thin black lines for both models and the fittings by AtomicJ-pyramid are shown in red whereas that of the trimechanic-3PCS model are in orange dashed lines. (**a**) System 1: the hard gel. AtomicJ-pyramid provides a value of 256 kPa for the effective Young's modulus, equivalent to a stiffness measure of 14.4 mN/m using an indentation transition of 113 nm (see Eq. 5), while our model obtains 230 and 236 kPa for Zone 1 and 2, and the corresponding k_S equals 3.91 and 20.0 mN/m, respectively. (**b**) System 2: the soft gel. The effective Young's modulus deduced from AtomiJ-pyramid is 29.5 kPa, equivalent to a stiffness of 4.37 mN/m at indentation depth of 298 nm. From the trimechanic-3PCS framework, we observed that $\hat{E}1$ = 54.4 and $\hat{E}2$ = 23.4 kPa with $k_{S,1}$ = 2.66 and $k_{S,2}$ = 6.52 mN/m, respectively. (**c**) System 3, only one value of effective Young's modulus was deduced from both methods, 45.5 kPa from AtomicJ-pyramid and 45.2 kPa from the trimechanic-3PCS model. (**d**) System 4, AtomicJ-pyramid yields $\hat{E}$ = 214 kPa, while the trimechanic-3PCS model reports five $\hat{E}$ values attributed to the five force/stiffness segments, ranging from 67.5 to 611 kPa (see **Fig. 3**). From the fitting results, one can see by adopting the conventional strategy for stiffness measure, AtomicJ-pyramid displays a poor fitting to the response of material in the initial indentation which is essential for accurately describing the elastic properties of material surface. $\hat{E}$ = 214 kPa from AtomicJ-pyramid is too high to account for the response of material in the initial indentation while it is too low to describe the impact of deepened depth brought on the stiffness magnitude for a material of heterogeneous elasticity.

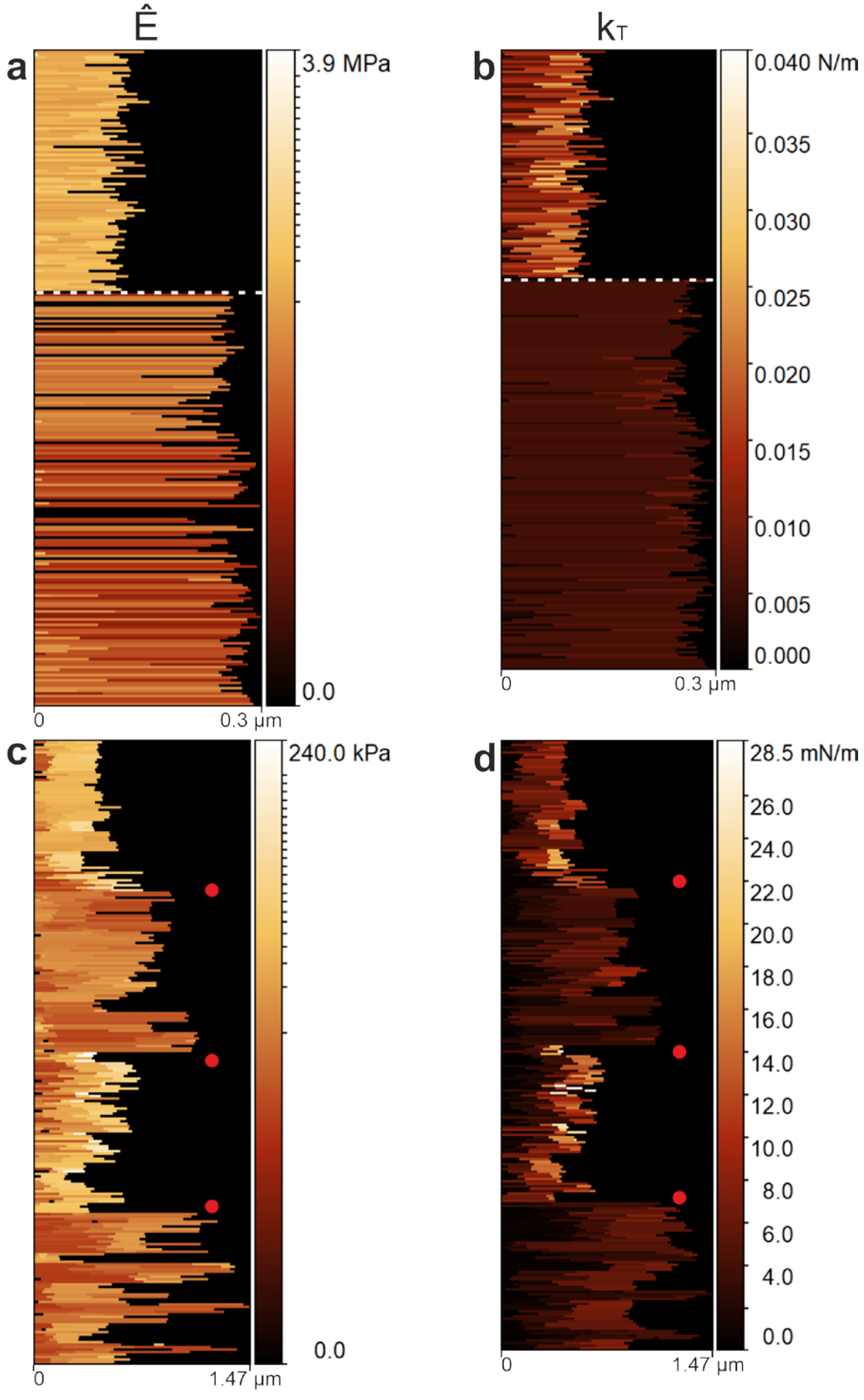
Ê
a
3.9 MPa
0.0
0
0.3 µm
kT
b
0.040 N/m
0.035
0.030
0.025
0.020
0.015
0.010
0.005
0.000
0
0.3 µm
c
240.0 kPa
0.0
0
1.47 µm
d
28.5 mN/m
26.0
24.0
22.0
20.0
18.0
16.0
14.0
12.0
10.0
8.0
6.0
4.0
0.0
0
1.47 µm

Figure S3: Bar graphs of effective Young's modulus and the stiffness measure k_T for polyacrylamide gels and plant roots. The horizontal-axis corresponds to the indented depth; the results of each indentation curve are represented with one line. The color bar on the right of the graph displays the value in the measured quantities. The graphics were generated using the Gwyddion software [5]. (**a**, **b**) The values of $\hat{E}$ and k_T of 91 sampled indentations for the hard gel as prepared for System 1, and beneath are 155 measurements for the soft gel for System 2. The separation of the two groups is marked by white dotted lines. By the naked eye, one can observed that the colors of $\hat{E}$ and k_T for the hard gel are much brighter than for the soft gel. Take the first depth-zone as an example, $\hat{E}_{\mathbf{hard}} = 2.96 \pm 4.02$ MPa (median = 2.27 MPa) vs. $\hat{E}_{\mathbf{soft}} = 0.41 \pm 0.62$ MPa (median = 0.32 MPa); $k_{T,\mathbf{hard}} = 9.96 \pm 4.90$ mN/m (median = 9.68 mN/m) vs. $k_{T,\mathbf{soft}} = 5.02 \pm 1.33$ mN/m (median = 5.51 mN/m). As for the first depth-zone, large standard deviations are observed for all depth-zones and underlie heterogeneity of cross-linker arrangement and inter-subgroup bonding properties. (**c**, **d**) The results of $\hat{E}$ and k_T of 248 indentation experiments on four different plant roots, maximum 64 curves for each root. The red spots mark the separation between the measurements on each roots. We observed that the values of $\hat{E}$, k_T and indentation length fluctuate widely, yet they vary more homogeneously within the same plant root. Recall that these root tissues are living organisms, their physiological conditions continuously change, e.g. the growth rate. For the first depth-zone, the averaged $\hat{E} = 94.9 \pm 101$ kPa with a median value of 58.4 kPa, and $k_T = 12.3 \pm 17.8$ with the median of 4.1 (in mN/m).

1. S. L. Crick and F. C. Yin, *Biomech. Model. Mechanobiol.*, 2007, **6**, 199-210.
2. A. Savitzky and M. J. E. Golay, *Anal. Chem.*, 1964, **36**, 1627-1639.
3. H. Spath, *Cluster dissection and analysis theory, fortran programs, examples*, Ellis Horwood Limited, Chichester, 1985.
4. P. Hermanowicz, M. Sarna, K. Burda and H. Gabrys, *Rev. Sci. Instrum.*, 2014, **85**, 063703.
5. D. Nečas and P. Klapetek, *Cent. Eur. J. Phys.*, 2012, **10**, 181-188.